Development of texture and seismic anisotropy during the onset of subduction

J. F. Di Leo, A. M. Walker, Z. -H. Li, J. Wookey, Neil M. Ribe, J. -M. Kendall, Andrea Tommasi

Geochemistry Geophysics Geosystems G3

Article
Volume 15, Number 1
31 January 2014
doi: 10.1002/2013GC005032
ISSN: 1525-2027

Published by AGU and the Geochemical Society

Development of texture and seismic anisotropy during the onset of subduction

J. F. Di Leo
School of Earth Sciences, University of Bristol, Bristol BS8 2UU, UK (jd7479@bristol.ac.uk)

A. M. Walker
School of Earth and Environment, University of Leeds, Leeds, UK

Z.-H. Li
State Key Lab of Continental Tectonics and Dynamics, Institute of Geology, Chinese Academy of Geological Sciences, Beijing, China

J. Wookey
School of Earth Sciences, University of Bristol, Bristol, UK

N. M. Ribe
Laboratoire FAST, UPMC/Univ Paris-Sud/CNRS, Orsay, France

J.-M. Kendall
School of Earth Sciences, University of Bristol, Bristol, UK

A. Tommasi
Geosciences Montpellier, CNRS and Université Montpellier 2, Montpellier, France

[1] How reliable are shear wave splitting measurements as a means of determining mantle flow direction? This remains a topic of debate, especially in the context of subduction. The answer hinges on whether our current understanding of mineral physics provides enough to accurately translate between seismic observations and mantle deformation. Here, we present an integrated model to simulate strain-history-dependent texture development and estimate resulting shear wave splitting in subduction environments. We do this for a mantle flow model that, in its geometry, approximates the double-sided Molucca Sea subduction system in Eastern Indonesia. We test a single-sided and a double-sided subduction case. Results are compared to recent splitting measurements of this region by Di Leo et al. (2012a). The setting lends itself as a case study, because it is fairly young and, therefore, early textures from the slab's descent from the near surface to the bottom of the mantle transition zone—which we simulate in our models—have not yet been overprinted by subsequent continuous steady state flow. Second, it allows us to test the significance of the double-sided geometry, i.e., the need for a rear barrier to achieve trench-parallel subslab mantle flow. We demonstrate that although a barrier amplifies trench-parallel subslab anisotropy due to mantle flow, it is not necessary to produce trench-parallel fast directions per se. In a simple model of A-type olivine lattice-preferred orientation and one-sided subduction, trench-parallel fast directions are produced by a combination of simple shear and extension through compression and pure shear in the subslab mantle.

Components: 11,748 words, 13 figures, 1 table.

Keywords: seismic anisotropy; subduction; mantle flow; shear wave splitting.

Index Terms: 8170 Subduction zone processes: Tectonophysics; 8120 Dynamics of lithosphere and mantle: general: Tectonophysics; 3060 Subduction zone processes: Marine Geology and Geophysics; 8413 Subduction zone processes: Volcanology; 1207 Transient deformation: Geodesy and Gravity; 1213 Earth's interior: dynamics: Geodesy and Gravity; 1219 Gravity anomalies and Earth structure: Geodesy and Gravity; 1240 Satellite geodesy: results: Geodesy and Gravity; 1031 Subduction zone processes: Geochemistry; 3613 Subduction zone processes: Mineralogy and Petrology; 7240 Subduction zones: Seismology.

Received 10 September 2013; **Revised** 15 November 2013; **Accepted** 26 November 2013; **Published** 31 January 2014.

Di Leo, J., A. Walker, Z.-H. Li, J. Wookey, N. Ribe, J.-M. Kendall, and A. Tommasi (2014), Development of texture and seismic anisotropy during the onset of subduction, *Geochem. Geophys. Geosyst.*, *15*, 192–212, doi:10.1002/2013GC005032.

1. Introduction

[2] Various seismological methods have shed light on the structure of the Earth's interior. In the case of subduction zones, for example, traveltime tomography [e.g., *van der Hilst et al*., 1991] or the accurate locating of slab seismicity [e.g., *Gudmundsson and Sambridge*, 1998; *Gutscher et al*., 2000] can provide a first-order image of subducting slabs and—to some extent—the surrounding mantle (see *Lay* [1994], for a review). These methods do not, however, constrain mantle convection as such.

[3] Currently, our best diagnostic tool for determining in situ mantle flow direction is seismic anisotropy: the directional dependence of seismic wave speed. This is due to the fact that in a dry upper mantle, olivine deformation is permitted mainly by the motion of dislocations belonging to the (010)[100] slip system. For progressive simple shear, this leads to the development of lattice-preferred orientation (LPO) of olivine-rich rocks, with the *a* axes aligned parallel to the mantle flow direction and the *b* axes perpendicular to the shear plane [e.g., *Ribe*, 1989; *Babuška and Cara*, 1991; *Mainprice*, 2007]. This is known as A-type LPO, which is observed both in LPO development models [e.g., *Wenk et al*., 1991; *Tommasi et al*., 2000] and experimentally deformed peridotites [e.g., *Nicolas et al*., 1973; *Avé-Lallemant*, 1975; *Zhang and Karato*, 1995; *Bystricky et al*., 2000]. The strain-induced mineral textures affect seismic wave propagation, a fact that manifests itself in shear wave splitting. When traversing an anisotropic medium (e.g., the convective upper mantle), a shear wave splits into two orthogonally polarized shear waves traveling at different speeds. The two parameters describing shear wave splitting are the delay time between those two shear waves (δt) and the polarization of the faster wave (ϕ), which is determined by the symmetry axis of the medium. For A-type olivine LPO, ϕ is parallel to the olivine *a* axes for vertically traveling shear waves and, therefore, parallel to the direction of (horizontal) mantle flow.

[4] Measurements of shear wave splitting have frequently been used to infer mantle flow in subduction zones. Source-side *S* wave splitting has proven especially useful in constraining anisotropy in the subslab mantle [e.g., *Russo and Silver*, 1994; *Müller et al*., 2008; *Di Leo et al*., 2012a, 2012b; *Lynner and Long*, 2013]. A topic of debate, however, is the predominance of trench-parallel fast directions, which most authors ascribe to trench-parallel subslab mantle flow. This interpretation seems counterintuitive in light of the classic model of 2-D mantle flow in subduction systems [e.g., *McKenzie*, 1969].

[5] Furthermore, it has often been pointed out that caution needs to be exercised when directly inferring mantle flow direction from shear wave splitting fast orientations [e.g., *Ribe*, 1989; *Dawson and Wenk*, 2000]. This is especially the case in regions of density-driven mantle flow, such as subduction zones, where mantle flow velocities and trajectories do not necessarily parallel those of the overriding plate due to partial decoupling of plate and mantle, and sharp changes in flow direction may occur [e.g., *Jadamec and Billen*, 2010, 2012; *Di Leo et al*., 2012b].

[6] One approach to testing whether the prevalent translation between seismic anisotropy observations and mantle flow direction through mineral physics are correct is to simulate strain-induced LPO development and subsequently predict the resultant shear wave splitting. This technique has been successfully applied to subduction settings in a number of previous studies [e.g., *Hall et al*., 2000; *Blackman and Kendall*, 2002; *Lassak et al*., 2006; *Faccenda and Capitanio*, 2012, 2013].

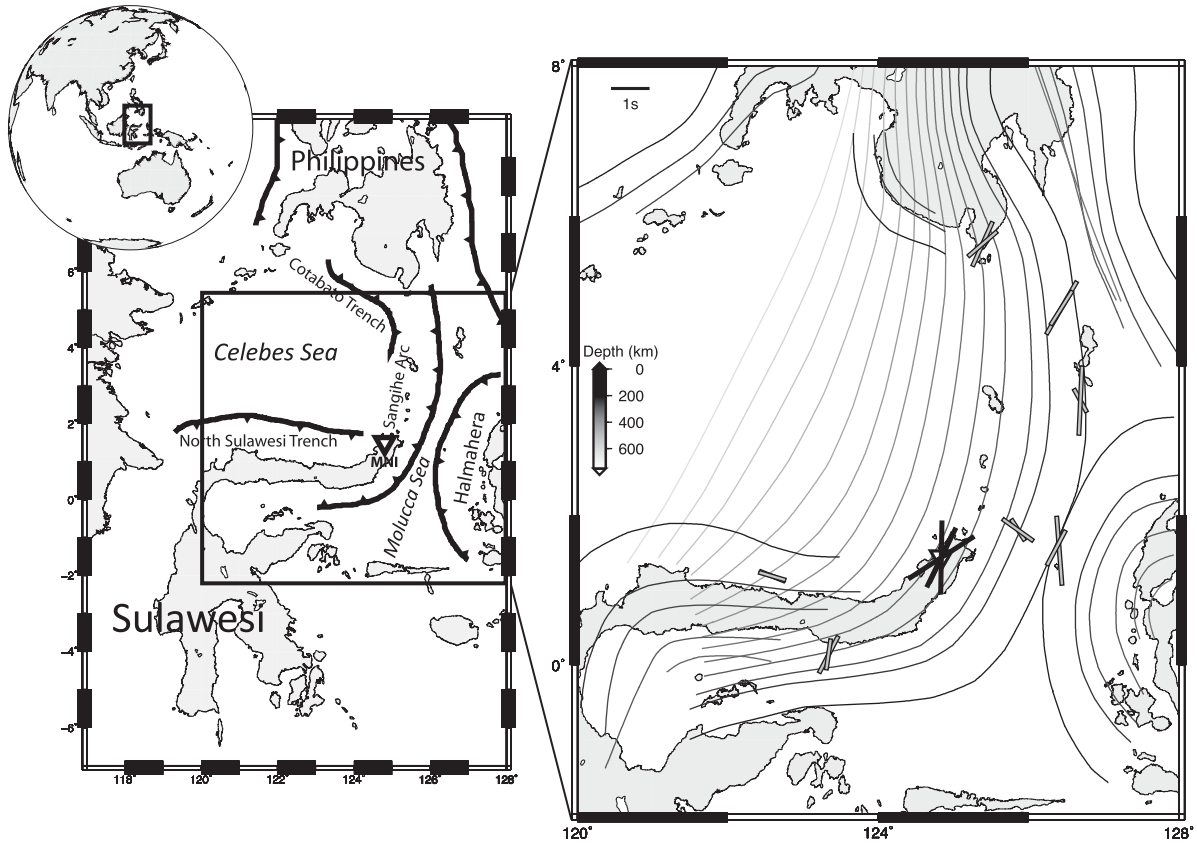

Figure 1. (left:) Map of the Sulawesi-Philippine region in SE Asia. Subduction zones are marked by lines with barbs pointing in the direction of slab dip (redrawn after *Hall and Nichols* [1990]; *Hall* [1997]; *Macpherson et al*. [2003]; *Djajadihardja et al*. [2004]). (right) Shear wave splitting results for the Sangihe subduction zone from *Di Leo et al*. [2012a]. Bars are oriented in the fast direction, their length is proportional to the delay time. Source-side results (gray) are plotted at the source, *SKS* results (black) are plotted at station MNI (inverted triangle). Slab contours (gray) [*Gudmundsson and Sambridge*, 1998] are in 50 km depth intervals. Both *SKS* and source-side splitting measurements predominantly show trench-parallel fast directions.

With the marked exception of recent work by *Faccenda and Capitanio* [2012, 2013], these earlier models have two significant shortcomings: (1) they are two-dimensional and (2) they only consider instantaneous, steady state mantle flow solutions.

[7] That mantle flow is far more complex (i.e., three-dimensional) beneath subduction zones has been demonstrated in numerous analogue experiments [*Buttles and Olson*, 1998; *Kincaid and Griffiths*, 2003; *Schellart*, 2004; *Funiciello et al*., 2006; *Druken et al*., 2011], numerical models [*Piromallo et al*., 2006; *Stegman et al*., 2006; *Lowman et al*., 2007; *Kneller and van Keken*, 2007; *Capitanio and Morra*, 2012; *Capitanio and Faccenda*, 2012], and seismic observations (see *Long* [2013] for a recent review), and this should therefore be taken into account. Equally important is the need to consider the entire strain history of the deformed mantle, as LPO textures are a function of the accumulated finite strain, but also the variation of flow velocity gradients along the path a volume of rock has traveled [e.g., *Kaminski and Ribe*, 2002].

[8] Here, we present an integrated model simulating subduction-history-dependent upper mantle LPO evolution and the resulting shear wave splitting. We compare results to observations from the Sangihe subduction zone in the Sulawesi-Philippine region.

[9] A shear wave splitting study was recently conducted on the Sangihe subduction zone (Figure 1) [*Di Leo et al*., 2012a]. This subduction zone is unique in that it is the western dipping part of the only present-day double-sided subduction system; the Molucca Sea microplate is also subducting eastward at the Halmahera trench. Through a combination of local *S*-, *SKS*-, and source-side

S-splitting observations, *Di Leo et al*. [2012a] inferred trench-perpendicular flow in the wedge above the subducting slab. The trench-parallel fast directions measured on the seaward side were attributed to trench-parallel escape flow beneath the slab in response to a volume decrease in the subslab mantle due to the double-sided subduction.

[10] In the following, we investigate whether shear wave splitting patterns observed in the mantle wedge and subslab region of the Sangihe subduction zone can be simulated in our model. For example, we test whether it is possible to produce trench-parallel fast directions from subslab mantle flow in a simple one-sided subduction model, where deformation is dominated by the motion of dislocations belonging to the (010)[100] slip system. We then compare these results to a two-sided subduction model to see how large an effect the unique double-sided geometry has.

[11] Unlike previous studies, we consider the entire subduction history, from initiation to stagnation at the 660 km discontinuity. This approach is appropriate for the Sangihe subduction zone, because it is fairly young (~25 Ma) [*Jaffe et al*., 2004] and the slab has only just reached the bottom of the mantle transition zone [*Tatsumi et al*., 1991; *Gudmundsson and Sambridge*, 1998]. In older subduction zones, where the slab has either been stagnating at the 660 km discontinuity for several million years or penetrated into the lower mantle, early textures developed during the slab's initial descent may eventually be destroyed by subsequent continuous mantle flow.

2. Methodology

[12] Our model to determine shear wave splitting due to strain-induced olivine LPO in a subduction setting consists of four steps: (1) we simulate mantle flow in a subduction zone that is designed to resemble the Sangihe subduction zone. Here, we test a single-sided and a double-sided subduction case, (2) texture evolution in the resulting subduction strain field is then modeled, (3) the corresponding aggregate elastic constants are determined, and (4) the resulting effective shear wave splitting is estimated.

2.1. The Mantle Flow Model

[13] To simulate mantle flow in a subduction zone, we use the 3-D numerical boundary element model (BEM) of *Li and Ribe* [2012]. The subducting plate is represented by a dense fluid sheet sinking in a horizontally infinite ambient mantle of lower viscosity. The model setup is similar to that of an analogue laboratory experiment [e.g., *Funiciello et al*., 2006]. However, an advantage of the boundary element method is that it allows for a laterally infinite mantle medium (i.e., without any sidewalls). In contrast, side boundaries always play a role in both laboratory experiments and numerical methods with finite-element or finite-difference approaches.

[14] We start with a small initial dip at one end of the plate, then the slab sinks under its own weight, i.e., due to slab pull (Figure 2). We define a rigid lower boundary at $H \approx 660$ km to represent the bottom of the mantle transition zone, at which the slab stagnates (Figure 2). The trench rolls back as the slab subducts. The upper boundary of the mantle medium is free-slip and impermeable. A thin lubrication layer (of the same viscosity η_1 as the mantle) prevents the entire plate from sinking. The initial geometry of the sheet is given by its width (w), thickness (h), the lengths of the plate (L), and slab (l), as well as the dip of the slab's leading edge. We define plate length as $(L + l) \approx 2040$ km and plate width as $w \approx 1020$ km. We choose these parameters to approximate the geometry of the Molucca Sea plate and Sangihe subduction zone.

[15] The mode of free subduction (i.e., trench advance or retreat, slab folding, etc.) depends on several factors, as previous numerical and experimental studies have shown [e.g., *Bellahsen et al*., 2005; *Di Giuseppe et al*., 2008; *Funiciello et al*., 2008; *Schellart*, 2008; *Ribe*, 2010; *Stegman et al*., 2010; *Li and Ribe*, 2012]. These factors include the plate/mantle viscosity ratio, $\gamma = \eta_2/\eta_1$, and the mantle depth/plate thickness ratio, H/h. Since we assume that $H \approx 660$ km and that the slab has a dip of ~60° [*Tatsumi et al*., 1991], then the preferred BEM solution has $\gamma = 200$ and $H/h = 7.8$, resulting in $h \approx 85$ km, which is a reasonable estimate of slab thickness in the Sangihe subduction zone [*Di Leo et al*., 2012a].

[16] The flow field evolves through time as the slab sinks. Figure 3 shows instantaneous flow at the final time step for the single-sided and the double-sided model.

2.2. Polycrystal Pathlines

[17] Since the mineral texture of a polycrystalline aggregate (hereafter referred to as "polycrystal") is the result of its entire strain history, we need to

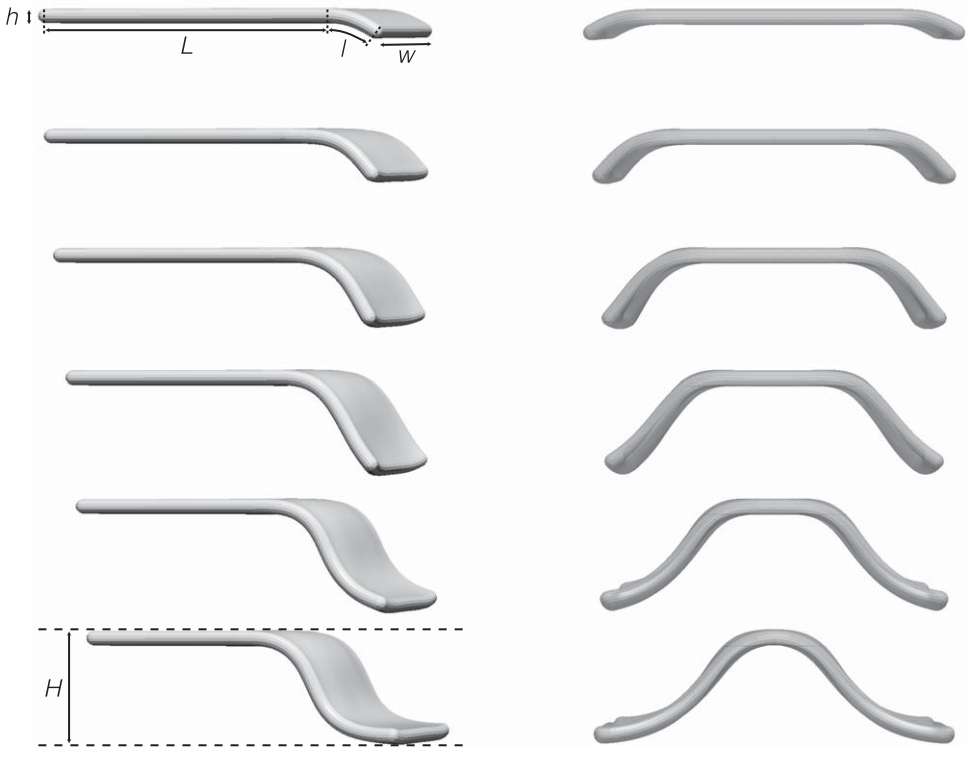

Figure 2. The (left) single-sided and (right) double-sided subduction model. A small initial dip is prescribed; after that, the slab sinks under its own weight ("slab pull"). The mantle layer has a rigid lower boundary at a depth (H) corresponding to 660 km to represent the bottom of the mantle transition zone, at which the slab stagnates. Thickness (h), width (w), and the lengths of the plate (L) and slab (l) are the same in the single-sided and double-sided model and approximate the geometry of the Molucca Sea plate.

follow the polycrystal's path from the beginning of the deformation phase to the point where we measure its texture. For our subduction model, this means that we need to trace the polycrystal from subduction initiation to stagnation of the slab at the lower boundary ("the 660"). We choose a number of passive tracer particles that end up in vertical columns at the end of the model run (i.e., at slab stagnation). These particle columns will represent vertically incident raypaths for the synthetic *SKS* waves in the subsequent calculation of shear wave splitting. The initial locations of the particles, however, are unknown. Therefore, we run the model backward to find these initial conditions (based on the reversibility of Stokes flow), and then forward again to calculate the textures.

[18] In each model (single-sided and double-sided), we consider 18 columns. The spacing between columns in a row is ~80 km. For the single-sided subduction case, we choose nine columns on the wedge side and nine on the seaward side to study anisotropic conditions above and below the slab, respectively. In the double-sided case, we choose one row of nine in the axial plane of the "anticlinal fold" of the plate and one row just off-center. The conditions in the wedge are the same in the single-sided and in the double-sided case. We only examine columns for half of the slab—from the center outward—as the model has mirror symmetry across the central vertical plane. Furthermore, the columns only extend down to $x_3 \approx 410$ km, since we are only examining texture development in olivine.

[19] We discretize each pathline into 150 steps of equal traveltime. At each step, we calculate the velocity gradient L (the change in velocity $\mathbf{v}$ with position $\mathbf{x}$) of the moving polycrystal:

$$L_{ij} = dv_i/dx_j, \tag{1}$$

which is the essential quantity for the following calculation of mineral textures, because it contains information about both macroscopic strain rate and rotation rate. L comprises a symmetric part, which is the strain rate tensor $\dot{\mathbf{E}}$, and a skew-symmetric part, which is the rotation rate tensor $\dot{\mathbf{W}}$:

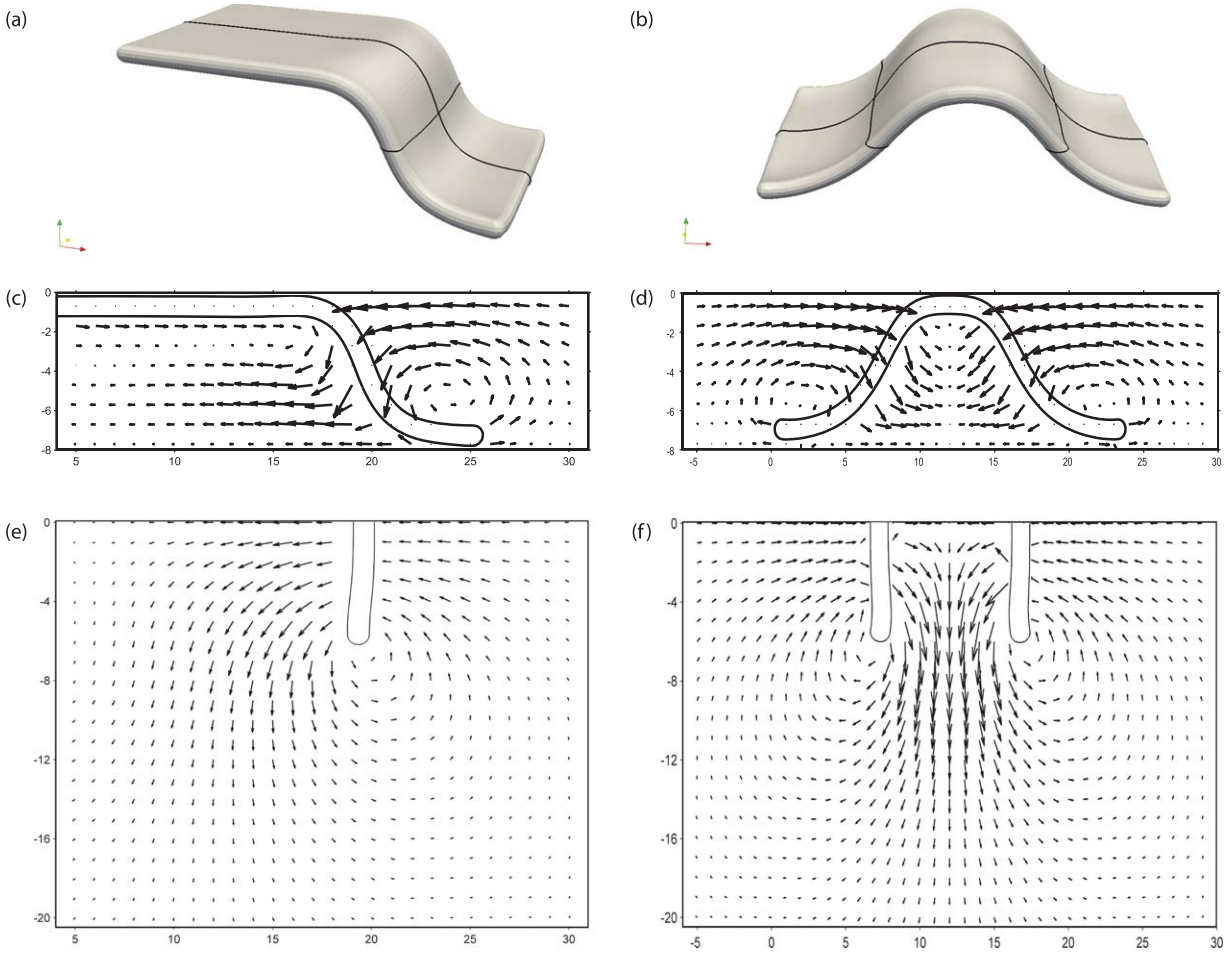

Figure 3. Instantaneous flow in the (left) single-sided and (right) double-sided model at the final time step. (c and d) Vertical cross-sections and (e and f) horizontal cross sections.

$$L=\dot{E}+\dot{W}, \tag{2}$$

where

$$\dot{E}_{ij}=(L_{ij}+L_{ji})/2, \tag{3}$$

$$\dot{W}_{ij}=(L_{ij}-L_{ji})/2. \tag{4}$$

[20] In order to better understand the pattern of macroscopic deformation, it can be useful to express the velocity gradient tensor on the principal axes of the strain rate tensor:

$$\mathrm{L}=\mathbf{R}\begin{pmatrix} \dot{e}_1 & -\frac{1}{2}\Omega_3 & \frac{1}{2}\Omega_2 \\ \frac{1}{2}\Omega_3 & \dot{e}_2 & -\frac{1}{2}\Omega_1 \\ -\frac{1}{2}\Omega_2 & \frac{1}{2}\Omega_1 & \dot{e}_3 \end{pmatrix}\mathbf{R}^{-1}, \tag{5}$$

where $\dot{e}_i$ and Ω_i are the three principal strain rates and components of the vorticity vector, respectively, and **R** is a transformation matrix with columns containing the three eigenvectors of the strain rate tensor.

2.3. Textural Evolution: The Viscoplastic Self-Consistent Approach

[21] LPO textures form when, due to externally imposed deformation, a significant number of crystals rotate and preferentially align within a polycrystalline aggregate (e.g., olivine crystals in a convective upper mantle). To calculate deformation-induced olivine textures, we use the anisotropic viscoplastic self-consistent (VPSC) model of *Lebensohn and Tomé* [1993]. The key idea is that each grain is treated as an ellipsoidal inclusion in a homogeneous effective medium (HEM), the properties of which are given by the average properties of the entire polycrystalline aggregate. Inputs to this model are the macroscopic strain rate tensor, $\dot{\mathrm{E}}$, and parameters

describing how individual slip systems permit single crystal deformation in response to grain-scale stress, σ. The strain rates for each crystal, $\dot{\varepsilon}$, the macroscopic stress, Σ, and the interaction tensor, M, are calculated iteratively for each time step along each pathline to yield a self-consistent solution to the equation:

$$\dot{\varepsilon}_{ij} - \dot{E}_{ij} = -\alpha M_{ijkl}(\sigma_{kl} - \Sigma_{kl}), \quad (6)$$

where the parameter α describes the interaction between the HEM and the grains. In the upper bound or *Taylor* [1938] model $\alpha = 0$, whereby strain is equal in each grain and hence homogeneous throughout the polycrystal, meaning that each crystal deforms identically, irrespective of its orientation. For this to be viable without opening any voids at grain boundaries, a crystal requires a minimum of five independent slip systems [*von Mises*, 1928], which is not the case for olivine. We therefore add two auxiliary slip systems with extremely high critical resolved shear stresses (Table 1). Texture development is not affected by these extra slip systems. With increasing α, stresses in each grain become more similar. We here choose $\alpha = 1$ in agreement with *Lebensohn and Tomé* [1993] tangent model. Once the self-consistent solution is found and the shear rate for each slip system in each grain is known, it is possible to compute the rate of rotation of each crystal due to dislocation accommodated by plastic deformation. Differences in this plastic rotation rate lead to the development of an LPO, while adding the macroscopic rotation allows the texture to rotate as a whole.

[22] Each polycrystal in our model consists of 500 initially randomly oriented grains. The orientations are denoted by three Euler angles (φ_1, Φ, φ_2), which give the rotation of the crystal lattice from the external Cartesian frame used for the flow modeling. The corresponding velocity gradient is applied to each polycrystal at each step along its pathline. At its final point in the vertical column the polycrystal has therefore recorded the entire strain history of the subduction process. The potentially active olivine slip systems, their critical resolved shear stresses (CRSS), and stress exponent (n) used here are listed in Table 1. Starting with a random distribution, the textures develop gradually along the 150 points of the pathline. The textures obtained from the VPSC calculations are represented by crystal orientations for each of the 500 grains. At the finishing point of the pathline, these new Euler angle triplets are then used to calculate the effective elastic constants for the textured polycrystalline aggregates by Voigt-Reuss-Hill averaging the single crystal olivine elasticity tensors over all the crystal orientations [e.g., *Mainprice et al*., 1990; *Walker et al*., 2011; *Walker and Wookey*, 2012].

Table 1. Olivine Slip Systems, Their critical Resolved Shear [from *Wenk et al*., 1991][a]

Slip System	CRSS	n
(010)[100]	0.4	3
(001)[100]	0.4	3
(010)[001]	1.0	3
$\{110\}\langle 1\bar{1}0\rangle$	5.0	3
$\{021\}\langle 1\bar{1}2\rangle$	5.0	3

[a]Note that two auxiliary slip systems must be invoked to fulfill von Mises' criterion.

[23] A limitation of the VPSC model is that it assumes crystallographic axes rotations (which lead to LPO development) to result exclusively from slip on a number of fixed slip planes. Other potentially texture-producing or texture-modifying processes such as diffusion creep, grain boundary sliding, grain boundary dislocation climb, or dynamic recrystallization are not taken into account.

[24] Recrystallization—through grain growth (boundary migration) and/or grain nucleation—is likely to occur at high temperatures and high strains [*Carter*, 1976; *Karato*, 1988]. Several experimental and numerical studies have focused on how recrystallization may affect LPO of olivine and enstatite, the two dominant upper mantle minerals [e.g., *Nicolas et al*., 1973; *Karato*, 1988; *Zhang and Karato*, 1995; *Wenk and Tomé*, 1999; *Kaminski and Ribe*, 2001; *Blackman et al*., 2002]. Natural and experimental samples appear to indicate that at large strain, recrystallization produces local misorientations, which can dilute the overall LPO [e.g., *Nicolas et al*., 1973; *Karato*, 1988; *Bystricky et al*., 2000; *Zhang et al*., 2000; *Falus et al*., 2011]. At modest strain, recrystallization can accelerate LPO formation [e.g., *Zhang and Karato*, 1995; *Zhang et al*., 2000]. However, *Tommasi* [1998] noted that by disregarding dynamic recrystallization, VPSC simulations tend to overestimate LPO intensity for high strains, but correctly predict LPO patterns. Moreover, *Wenk and Tomé* [1999] came to the conclusion that although there are differences between dislocation glide and recrystallization textures, the effects on seismic wave propagation are negligible.

[25] Although the oceanic upper mantle is considered to typically consist of ~70% olivine and

~30% enstatite [e.g., *Dick et al*., 1984; *Boudier and Nicolas*, 1995; *Jaraslow et al*., 1996], we run our simulations with 100% olivine. This will overestimate the overall LPO intensity and hence the aggregate seismic anisotropy [*Mainprice and Silver*, 1993]. For a 70/30 olivine/enstatite ratio, *Blackman et al*. [2002] determined a 23% reduction of shear wave splitting in the maximum splitting direction. This is partly due to the fact that for single crystals, *S* wave anistropy of enstatite is markedly different to that of olivine. Furthermore, deformational behavior of the two minerals is dissimilar. Since olivine dominates quantitatively and is the mechanically weaker mineral, it controls deformation and hence LPO development of upper mantle peridotite. However, enstatite does not modify olivine LPO patterns [*Wenk et al*., 1991; *Tommasi*, 1998]. Therefore, while using pure olivine in our simulations overestimates the aggregate anisotropy intensity, the shear wave splitting fast directions should be robust.

2.4. Estimating Shear Wave Splitting

[26] From the obtained elasticity tensors, we can now determine the effective shear wave splitting arising from upper mantle olivine LPO that one would measure if seismometers were installed at the surface. Since a variation of splitting parameters with backazimuths can be indicative of multiple layers of anisotropy [*Silver and Savage*, 1994], we measure shear wave splitting for vertically incident *SKS* phases with polarizations (corresponding to backazimuth) between 0° and 180° in steps of 5° for each column.

[27] We use two approaches. First, we follow the method of *Silver and Savage* [1994] for shear wave splitting in the case of multilayer anisotropy [see also *Walker and Wookey*, 2012]. When an incident shear wave traverses multiple layers of anisotropy along its path to the receiver, every layer will cause that wave to split. However, the frequency is most likely too low to produce identifiable pulses for each layer. What is observed instead is apparent or effective splitting, which is a combination of all the individual splitting operators. In the case of our model, that means that every textured olivine aggregate in the final columns (e.g., Figure 4) represents a layer of anisotropy. Splitting operators are determined for each layer, and the effective splitting operators are retrieved for each column, i.e., each *SKS* wave.

[28] In the second method we use to calculate the effective splitting parameters, the individual splitting operators along the vertical column (i.e., the *SKS* raypath) are applied in sequence to an unsplit first-derivative Gaussian wavelet; then the effective splitting operator that minimizes the second eigenvalue of the covariance matrix of the result is determined [*Silver and Chan*, 1991]. This ray theory approach is similar to that implemented by *Bonnin et al*. [2012]. The average difference between these results and those obtained with the *Silver and Savage* [1994] method is 9.10° for fast direction and 0.37 s for delay time, which is within typical error of shear wave splitting measurements of nonsynthetic data. Hereafter, we show results obtained with the second method.

3. Results

[29] In the following, we present the olivine LPO textures in pole figures that are upper hemisphere orientation density plots (scaled in multiples of uniform distribution, MUD). The reference frame—both for the subduction model and the pole figures—is such that the *y* direction is parallel and the *x* direction is perpendicular to the trench, with the slab subducting toward positive *x* (Figure 4). For reference, supporting information Figure S1[1] shows pole figures for end-member cases of simple shear, pure shear, axial compression, and axial extension deformation.

3.1. Textures

3.1.1. Single-Sided Subduction: The Mantle Wedge

[30] Figure 5 shows textures in the center of the mantle wedge at the end of the model run. Near the surface, there are well-developed textures with strong orientation of olivine *a* axes horizontal and perpendicular to the trench (i.e., parallel to the *x* direction). The *b* and *c* axes show a girdle distribution. The textures are indicative of axial extension in the *x* direction. Simple shear textures are clearly evident at the bottom of the wedge, nearest the slab, with the shear plane dipping approximately parallel to the slab. In the interior of the wedge, however, textures are more dispersed without any clear distribution maxima. The resulting picture approaches, perhaps unsurprisingly, that of 2-D mantle wedge corner flow.

[31] Textures at the wedge-side edge of the slab (Figure 6) are most clearly developed near the surface: The *a* axes show a strong maximum that is

[1]Additional supporting information may be found in the online version of this article.

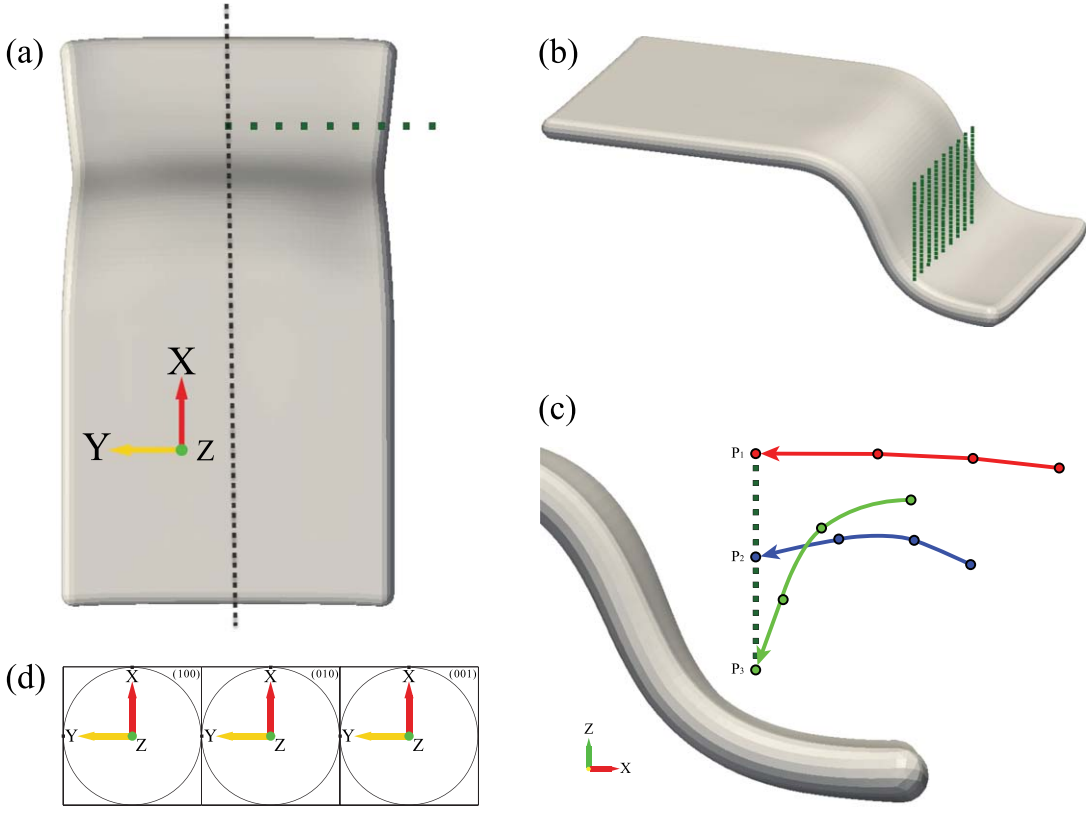

Figure 4. Particle columns, pathlines, and the model reference frame. Dark green points mark the polycrystalline olivine aggregates in their final position at the end of the model run. The columns will represent vertically incident raypaths for the synthetic *SKS* waves in the subsequent measurement of shear wave splitting. (a) Map view of the slab, which subducts toward positive *x*. Dark green squares denote the wedge-side particle columns (alternatively, they can be viewed as marking seismic station locations). Note that, we only examine columns for half of the slab, as the model has mirror symmetry across the central vertical plane (dashed line). (b) The wedge-side columns. (c) Example of pathlines for three olivine polycrystals (red: P_1, blue: P_2, and green: P_3) in the vertical symmetry plane of the subduction model, from their starting to their final positions (and two intermediate steps). This shows the complex geometry of flow in the mantle wedge during the slab's descent. P_1 is drawn across nearly horizontally. However, P_2 is actually drawn from a deeper initial point than P_3, despite finishing above it. (d) Olivine LPO textures are presented in pole figures that are upper hemisphere orientation density plots. The reference frame—both for the subduction model and the pole figures—is such that the *y* direction is trench parallel and the *x* direction is trench perpendicular.

nearly trench parallel, with a slight dip toward the slab, and the *b* and *c* axes are both exhibiting a girdle distribution. The reason for the upper part of the particle column being more strongly textured is that throughout the subduction process (i.e., the slab's descent from the near surface to the "660") it has been subjected to more deformation than the lower part of the mantle.

3.1.2. Single-Sided Subduction: The Subslab Mantle

[32] Figure 7 shows textures in the center of the subslab mantle. For the most part, there is no clear trench-parallel trend. Only toward the bottom of the column (above the 410 km discontinuity) do the *a* axes exhibit a trench-parallel maximum. In the rest of the column, there is a great dispersion of olivine *a* axes, but a maximum of weak *b* axes in the in the *z* direction. The textures indicate a combination of simple shear—with a horizontal, *x*-*y* shear plane—and compression.

[33] Textures at the seaward-side edge of the slab (Figure 8) also do not show a strong trench-parallel LPO. The *a* axes have a maximum that is trench oblique, with a 90° rotation occurring from the top to the bottom of the column.

3.1.3. Double-Sided Subduction: The Subslab Mantle

[34] Textures developed during double-sided subduction, on the other hand, show very strong

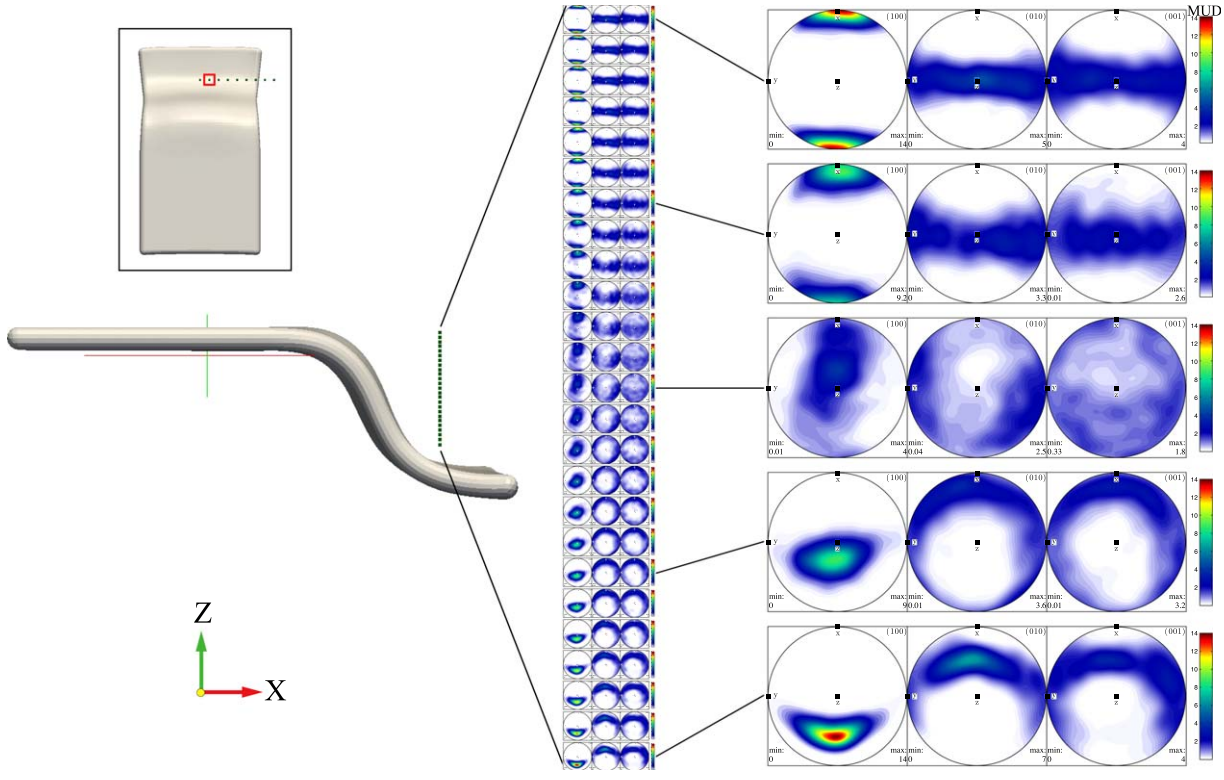

Figure 5. Textures in the center of the mantle wedge. Pole figures are upper hemisphere orientation density plots (scaled in multiples of uniform distribution, MUD). Examples of the pathlines of the uppermost, lowermost, and middle olivine polycrystals (dark green squares) are shown in Figure 4. Near the surface, textures are well developed with strong horizontal orientation of olivine *a* axes perpendicular to the trench. The *b* and *c* axes show a girdle distribution. The textures indicate axial extension in the *x* direction. Simple shear textures are evident at the bottom of the wedge, above the slab, with the shear plane dipping parallel to the slab. In the interior of the wedge, textures are more dispersed without any clear orientation maxima.

trench-parallel *a* axes maxima. Beneath the center of the plate (Figure 9), textures have a clear *a* axes maximum parallel to the two trenches. The maximum of the *b* axes is in the *x* direction, i.e., perpendicular to the trench. Since we impose a model that is designed to generate A-type olivine LPO for simple shear, this means that the shear plane is the *y*-*z* plane (i.e., the axial plane of the "anticlinal fold" of the plate). At the edge of the slab (Figure 11), textures are similar, albeit with less pronounced maxima.

[35] Away from the "anticlinal fold plane" (Figure 10), trench-parallel *a* axis maxima become more pronounced from the top of the column to the bottom, and there is a change from horizontal simple shear to pure shear and extension.

3.2. SKS Splitting

[36] The resultant aggregate *SKS* splitting measurements (averaged over all backazimuths) are shown in Figure 12. The black bars are oriented in the fast direction (ϕ). Their length is proportional to the delay time (δt). As previously mentioned, delay times are slightly higher than they would occur in nature due to the absence of enstatite and dynamic recrystallization in our models. However, of greater importance here are the relative differences in δt between the different regions of mantle flow (e.g., between the wedge and the subslab mantle) and between the two subduction models.

[37] In the mantle wedge, delay times are between 2.2 and 4.9 s. In the center of the slab, fast directions are trench perpendicular, which is in accordance with the calculated textures at that column (Figure 5). Toward the edge of the slab, however, there is a clockwise rotation in ϕ until, at the outermost column, ϕ is nearly trench parallel.

[38] What is immediately noticeable are the stark differences in splitting measurements of the subslab mantle. In the single-sided model, time lags are markedly smaller (0.3–1.5 s) than in the double-sided model (2.2–4.9 s). Furthermore,

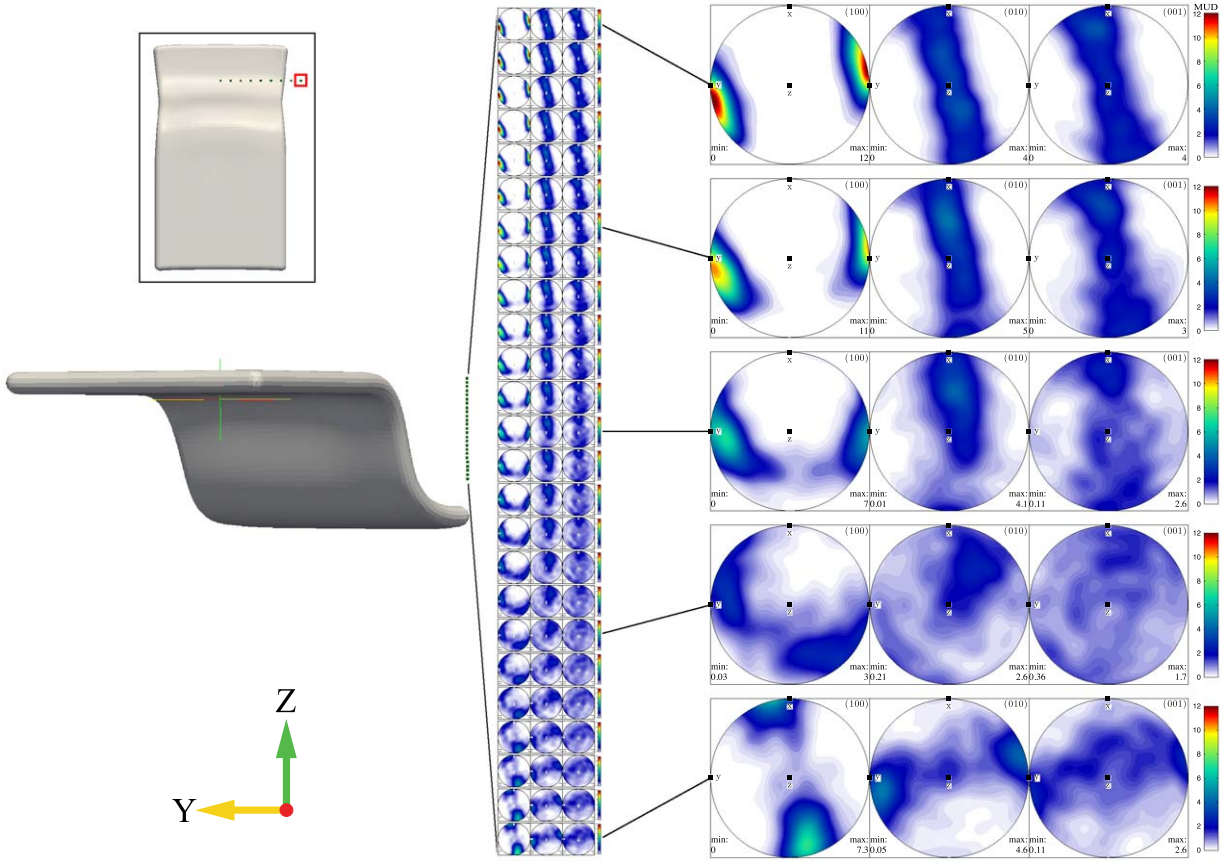

Figure 6. Textures at the wedge-side edge of the slab are strongest near the surface: The *a* axes show a clear maximum that is nearly trench parallel, with a slight dip toward the slab; the *b* and *c* axes both exhibit a girdle distribution. The upper part of the polycrystal column is more strongly textured, because, throughout the slab's descent from the near surface to the "660," it has been subjected to more deformation than the lower part of the mantle.

although there is a trench-parallel trend in ϕ in the single-sided case, it is much more pronounced in the double-sided case, as expected from the associated textures (Figures 7 and 9).

[39] In some regions of the model there is a strong variation of splitting parameters with backazimuth. For example, in the subslab mantle of the single-sided model, there is a 90° periodicity (supporting information Figure S2), which is indicative of two or more layers of anisotropy [*Silver and Savage*, 1994]. It is not surprising when looking at the change in texture throughout the column (Figure 7), from trench-perpendicular *a* axis maxima at the top to trench-parallel *a* axis maxima at the bottom. This is noteworthy. In real data, we rarely have complete backazimuthal coverage—be it due to an unfortunate arrangement of sources or paucity of high-magnitude earthquakes during temporary station deployments—and it may be that some of the global variation we see in subduction zone splitting results from a combination of imaging geometry and multilayer anisotropy. For example, in the case of the seaward-side station, for which textures are shown in Figure 7, trench-parallel or trench-perpendicular backazimuths would both result in perfectly trench-perpendicular fast directions (supporting information Figure S2). However, for a backazimuth of 60°, for example, the resulting fast direction would be approximately −45° and, therefore, trench oblique.

4. Discussion

[40] The modeling of history-dependent textures in an evolving subduction zone provides several important insights, and although the Molucca Sea is—to the best of our knowledge—currently the only locality of two-sided subduction, the comparison with subslab textures developed during double-sided subduction yields interesting implications.

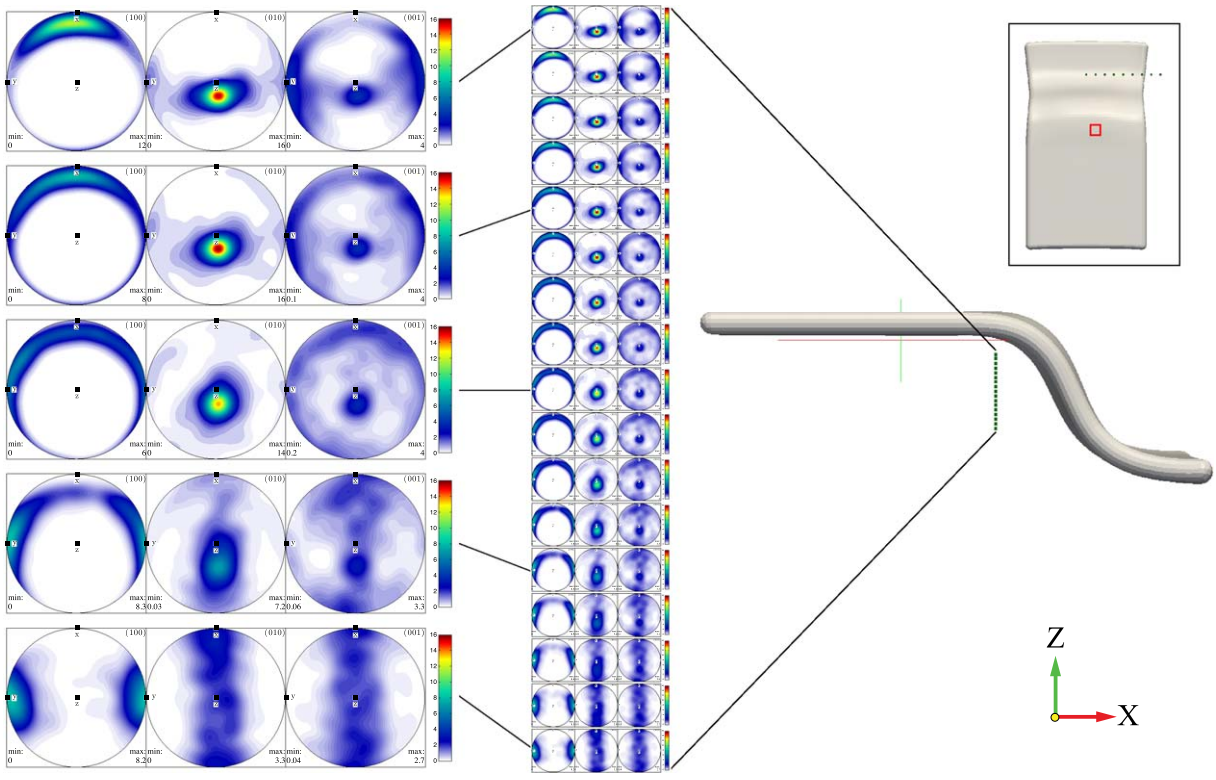

Figure 7. Textures in the center of the subslab mantle. Only toward the bottom of the column (above the "410") do the *a* axes exhibit a trench-parallel maximum. In the upper part of the column, there is a dispersion of olivine *a* axes, but a maximum of *b* axes in the in the *z* direction. The textures indicate a combination of simple shear (with a horizontal, *x*-*y* shear plane) in the upper part of the column and a compressional/extensional regime at the bottom. The simple shear component stems from divergent flow of the mantle escaping slab rollback horizontally, whereas the compression-extension component is due to the slab collapsing onto the mantle in the vertical direction.

4.1. Seismic Anisotropy in the Mantle Wedge

[41] The calculated textures in the central part of the wedge (Figure 5) show strong horizontal *a* axes maxima perpendicular to the trench in the upper 150 km of the mantle. Moving downward in the olivine aggregate column, one can observe a rotation of *a* axes maxima toward a strong slab-dip-parallel maximum in the lower 100 km, just above the slab. In other words: shear is strongest in the upper 150 km of the mantle wedge and in the ~100 km above the subducting slab.

[42] That shearing is strong near the surface becomes clear when looking at the flow field (Figure 3c) and the pathlines for the midwedge in Figure 4. As the slab subducts, mantle material is only being drawn in horizontally. The material finishing closest to the slab, on the other hand, has been dragged down a significant distance. Nonetheless, the textures at the bottom of the column are parallel to the slab dip, not the traveled path. This is perhaps due to the fact that the immediate layer of mantle above the slab is dominated by progressive simple shear parallel to the slab, where shear stress and strain are extremely high and, thus, strong dip-parallel LPO can develop. Supraslab anisotropy due to progressive simple shear has been predicted by *McKenzie* [1979], *Ribe* [1989], and *Kendall and Thomson* [1993], observed in analogue models [e.g., *Buttles and Olson*, 1998] and, recently, in shear wave splitting data: *Di Leo et al.* [2012a] interpreted trench-perpendicular fast directions of local *S* splitting as being due to such shear layers of strong LPO atop the Molucca Sea slab in the Sangihe subduction zone.

[43] A common observation in shear wave splitting studies of subduction zones is that the interior of the wedge appears to be largely isotropic [e.g., *Polet et al.*, 2000; *Morley et al.*, 2006; *Piñero-Feliciangeli and Kendall*, 2008; *Hammond et al.*, 2010; *Di Leo et al.*, 2012a]. *Buttles and Olson*

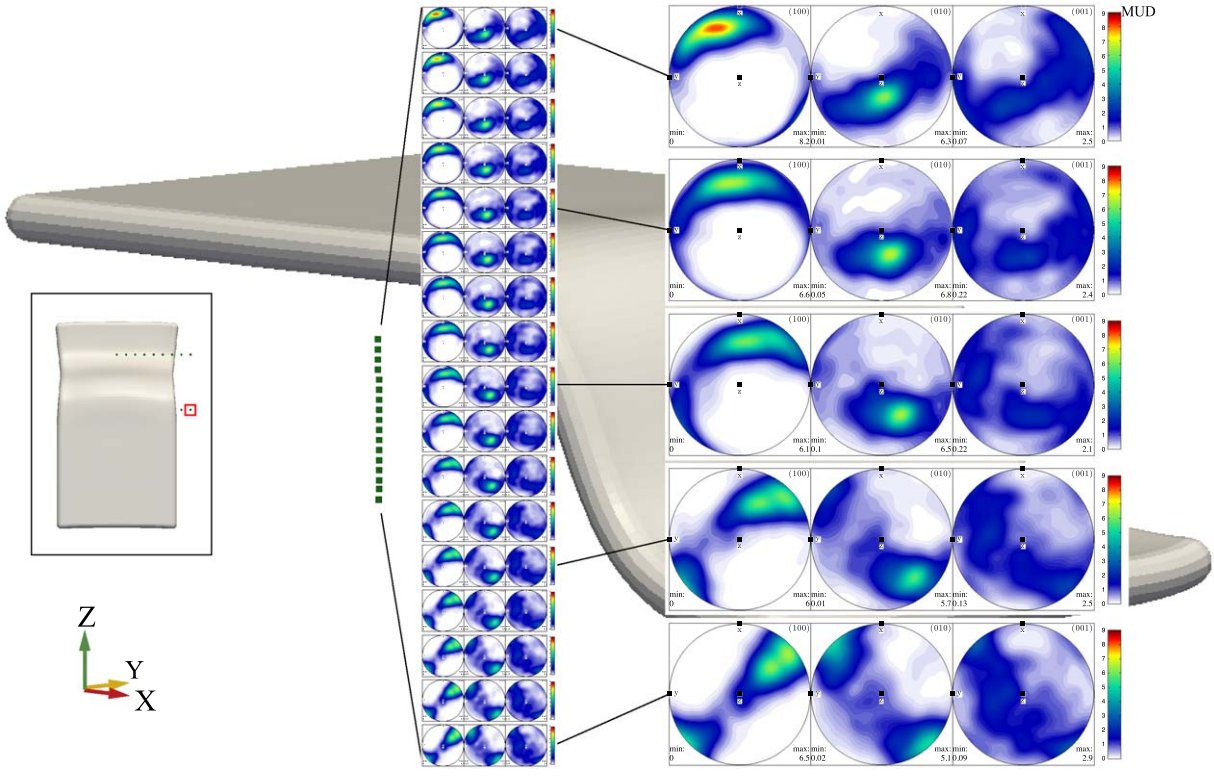

Figure 8. Textures at the seaward-side edge of the slab do not show strong trench-parallel orientations. The *a* axes have a maximum that is oblique to the trench, with a 90° rotation occurring from the top to the bottom of the column.

[1998] made similar observations in their analogue models; fast directions in the wedge interior were extremely variable, especially for steeply (>45°) dipping slabs. This is in good agreement with the textures we have calculated here (Figure 5): textures for the wedge interior (i.e., the middle of the column) show no strong preferred orientation.

[44] Overall, the anisotropy could be interpreted as "2-D corner flow." However, that term is misleading. "Corner flow" suggests a continuous, roughly triangular flow in the mantle wedge. Such a flow can be expected in an older subduction zone that has been stagnating at the bottom of the mantle transition zone for a prolonged period of time. What we calculate here are the early textures that develop as the slab subducts. A look at the pathlines of mantle material (Figure 4) shows that the flow during the early stages of subduction is not perfectly triangular, but rather more complex. Furthermore, Figure 4 shows flow in the central mirror plane of the slab. Moving toward the edges of the slabs, flow becomes even more complex and trench oblique, as evidenced by the textures (Figure 6) and shear wave splitting results (Figure 12).

4.2. Slab Edge Effects

[45] Toroidal flow around slab edges (from the underlying and surrounding mantle toward the wedge) has been observed in the immediate vicinity of slab terminations in numerical models [e.g., *Zhong et al*., 1998; *Piromallo et al*., 2006; *Stegman et al*., 2006; *Lowman et al*., 2007; *Faccenda and Capitanio*, 2013] and analogue laboratory experiments [e.g., *Kincaid and Olson*, 1987; *Buttles and Olson*, 1998; *Schellart*, 2004] and has been inferred from shear wave splitting data [e.g., *Civello and Margheriti*, 2004; *Currie et al*., 2004; *Di Leo et al*., 2012b]. Such return flow around the slab's edge is also evident in our models: in the flow field (Figure 3), in the textures (Figure 6), and in the fast directions (Figure 12). The toroidal flow develops very early in the subduction process, long before the slab reaches a lower boundary. Our modeling results suggest that, given the right source-receiver configuration, shear wave splitting can be employed as a tool for detecting toroidal flow.

4.3. Subslab Seismic Anisotropy

[46] We can describe the style of strain experienced by a polycrystal along its trajectory

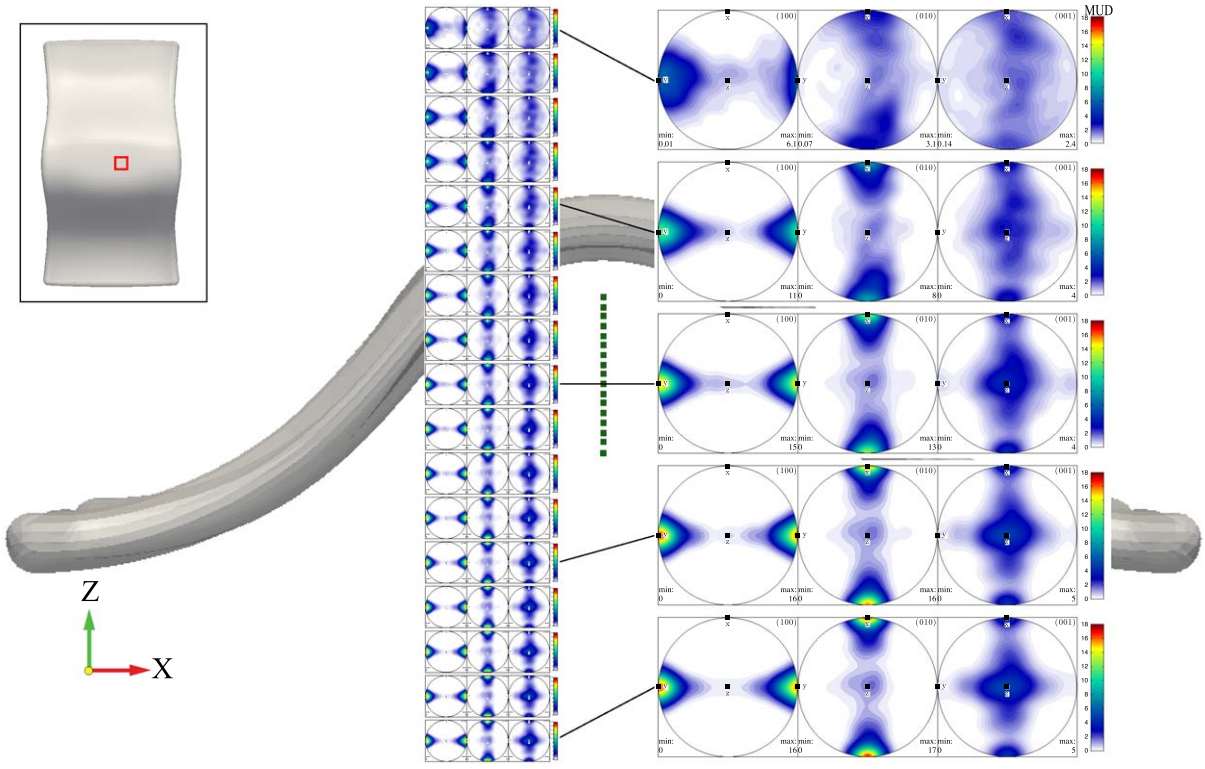

Figure 9. Textures in the subslab mantle (slab center) in the double-sided model show a very strong trench-parallel trend. Beneath the center of the plate, textures have an *a* axes maximum parallel to the two trenches. The maximum of *b* axes is perpendicular to the trenches. For A-type olivine LPO, this means that the shear plane is in the axial plane of the "anticlinal fold" of the plate (the *y*-*z* plane).

graphically in a manner based on the "Flinn diagram" [*Flinn*, 1962]. This allows us to visualize the history of deformation that leads to the development of a particular texture and seismic anisotropy, and understand the importance of a changing flow field for our results. Figure 13 shows examples for subslab polycrystals of the single- and the double-sided subduction model. (See supporting information Figure S3 for a diagram of deformation in the wedge.) The horizontal axis is $x = (1 + \dot{e}_2)/(1 + \dot{e}_3)$ and the vertical axis $y = (1 + \dot{e}_1)/(1 + \dot{e}_2)$, where $\dot{e}_1$, $\dot{e}_2$, and $\dot{e}_3$ are the largest positive, intermediate, and minimum negative eigenvalues of the strain rate tensor $\dot{\mathrm{E}}$, respectively, and $\dot{e}_1 + \dot{e}_2 + \dot{e}_3 = 0$ by incompressibility. Points plotting on the line $x = y$ correspond to plane strain deformation; the vertical axis ($x = 0$) corresponds to uniaxial extension, and the horizontal axis ($y = 0$) to uniaxial compression. The points represent the 150 time steps and are color coded by the vorticity number, , which is the absolute value of the vorticity vector normalized by the second invariant of the strain rate tensor. In plane strain ($x = y$), $= 0$ for pure shear, $= 1$ is consistent with simple shear, and > 1 signifies deformation in which vorticity dominates over shear.

[47] In the upper part of the subslab mantle (Figures 13a and 13b), the dominant type of deformation is simple shear. However, in the double-sided model, there is also a significant amount of compression. The middle of the column is where the single-sided and the double-sided model differ the most in their strain history. In the single-sided case, axial compression clearly dominates, whereas in the double-sided case, simple shear appears to be the primary type of deformation. At the bottom of the column of the single-sided model, deformation starts off with pure shear and compression and then transitions to extension. In the double-sided model, pure shear and extension are clearly the dominant type of strain.

[48] Several authors have proposed 3-D mantle flow models in subduction zones that involve trench-parallel flow beneath the slab [e.g., *Russo and Silver*, 1994; *Piñero-Feliciangeli and Kendall*, 2008; *Long and Silver*, 2008, 2009] to account for observations of trench-parallel fast

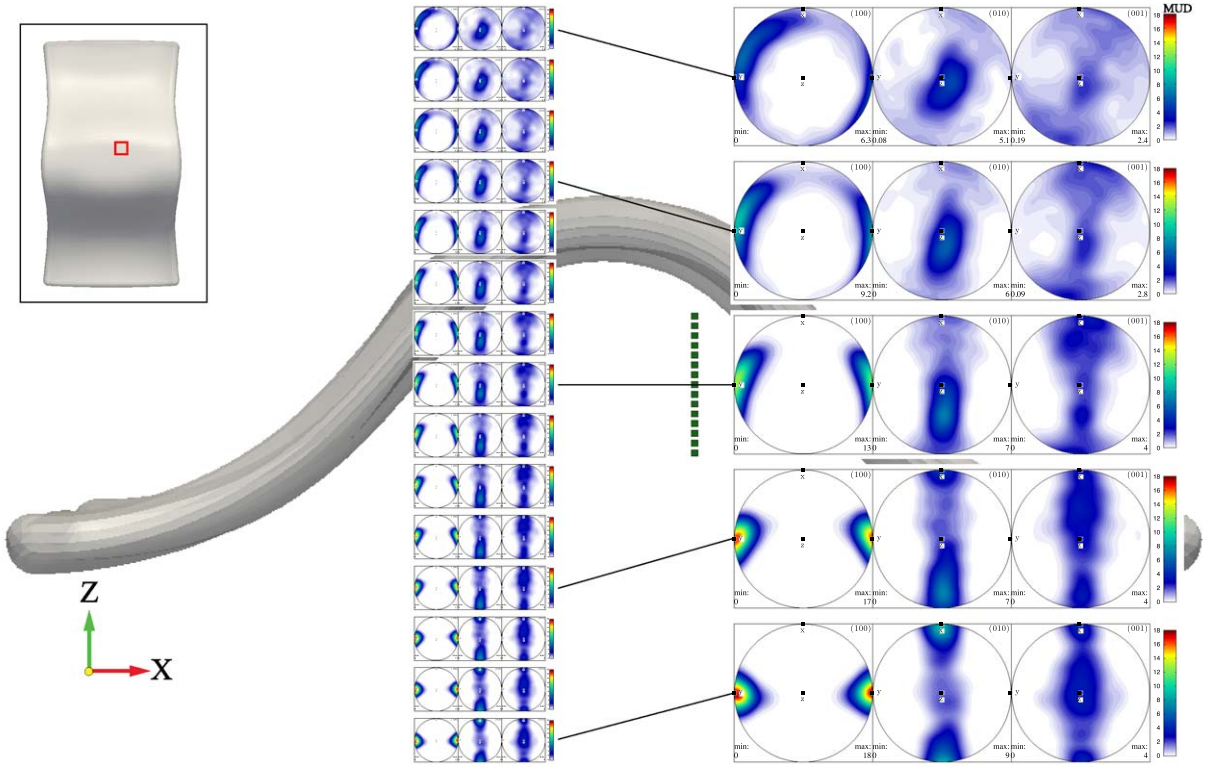

Figure 10. Textures in the subslab mantle (away from the "anticlinal fold plane"). From top to bottom, trench-parallel *a* axis maxima become more pronounced, and there is a change from horizontal simple shear to pure shear extension.

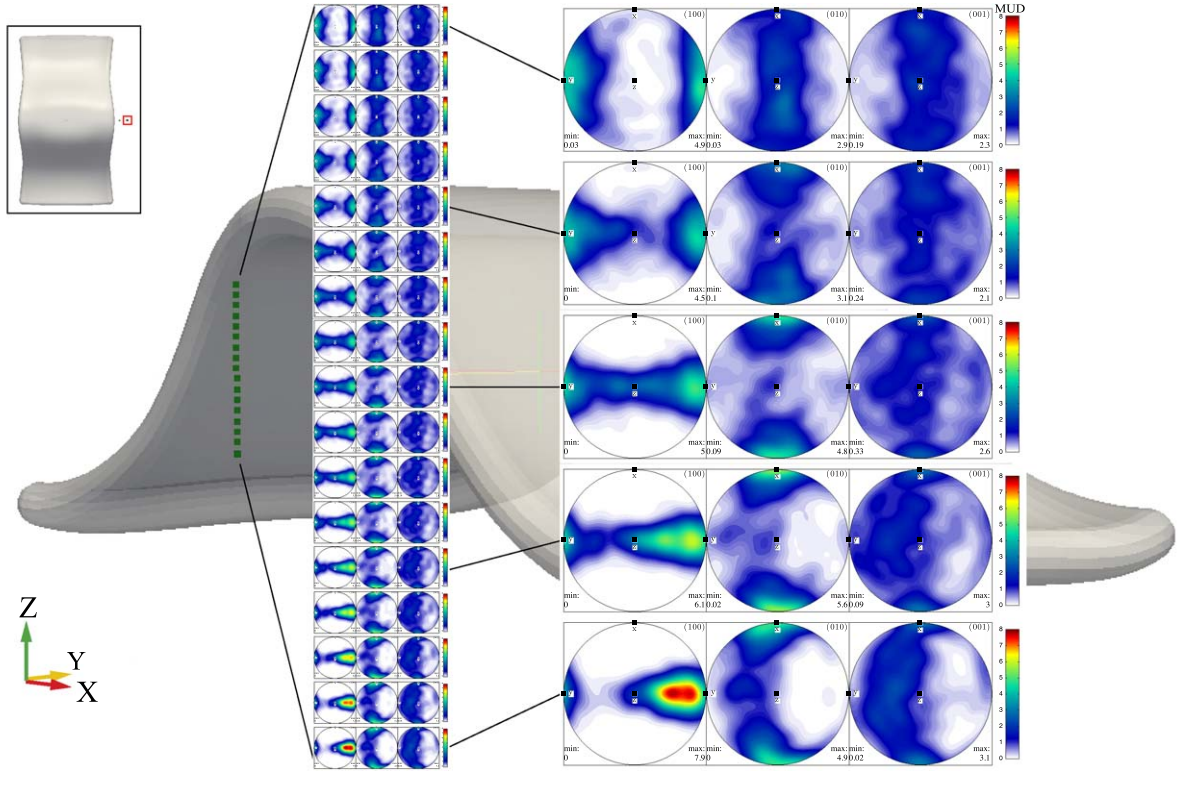

Figure 11. Textures in the subslab mantle (slab edge) in the double-sided subduction model are similar to those beneath the slab center (Figure 9), but with less pronounced maxima.

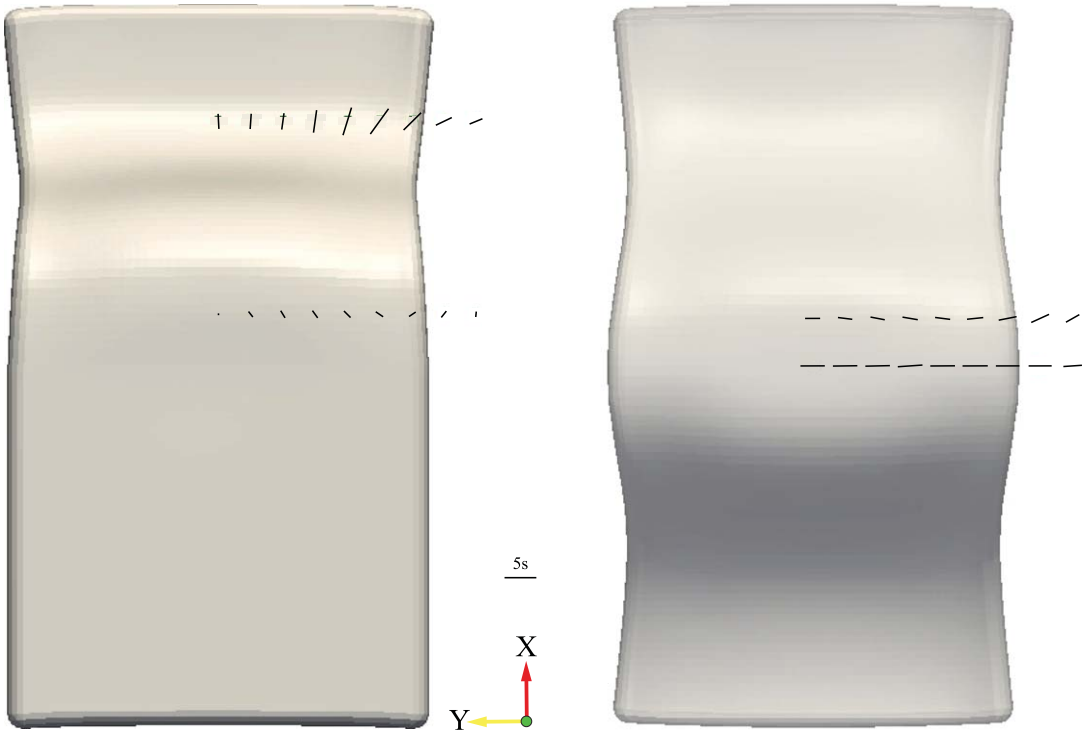

Figure 12. *SKS* splitting results for (a) single-sided and (b) double-sided subduction. The black bars are oriented in the fast direction, their length is proportional to the delay time. Notice the striking differences in splitting measurements of the subslab mantle: In the single-sided model, time lags are significantly smaller (0.3–1.5 s) than in the double-sided model (2.3–4.1 s). Moreover, although there is a trench-parallel trend in ϕ in the single-sided case, it is much more pronounced in the double-sided case, as expected from the associated textures (Figures 7 and 9).

directions. Two prerequisites for such a model are a barrier to flow behind the slab and parallel to the trench as well as a barrier to flow at depth. The latter is given by the 660 km discontinuity, which, although not yet fully understood, is believed to act as a semipermeable barrier [e.g., *Tackley*, 2008]. In the double-sided model, the second slab acts as a trench-parallel barrier. The only escape route for the mantle between the two slabs is, therefore, outward, parallel to the two trenches. This is evident from the flow field in our models (Figure 3f). The calculated textures support this assumption (Figures 9–11), showing well-developed olivine *a* axes maxima parallel to the trenches. This is in agreement with shear wave splitting observations by *Di Leo et al*. [2012a]. However, it is also clear from the textures and the modified "Flinn diagrams" that trench-parallel extension caused by axial compression and pure shear adds to the development of trench-parallel splitting fast directions as well. The textures are, therefore, not simply a result of trench-parallel simple-shear flow of the mantle being shoved out of the way by the subducting slab.

[49] What is significant, perhaps, is the development of subslab trench-parallel ϕ in the single-sided case. We demonstrate that this is achievable with the simplest of models—i.e., pure dry olivine deforming so as to generate an A-type LPO in progressive simple shear—due to the combination of simple-shear strain induced by trench-parallel flow in the upper part of the subslab mantle, but also compression leading to trench-parallel extension in the lower part. Furthermore, there is no need to invoke other mechanisms such as a pressure-induced transition in the olivine slip systems to B-type LPO [*Couvy et al*., 2004; *Raterron et al*., 2007; *Carrez et al*., 2008; *Jung et al*., 2009; *Raterron et al*., 2009; *Walker et al*., 2010]. *Faccenda and Capitanio* [2013] have recently pointed out the importance of pure shear and extension in the development of trench-parallel subslab seismic anisotropy. Our results further show that a barrier to flow behind the slab significantly amplifies trench-parallel subslab anisotropy, but it is not a prerequisite for it.

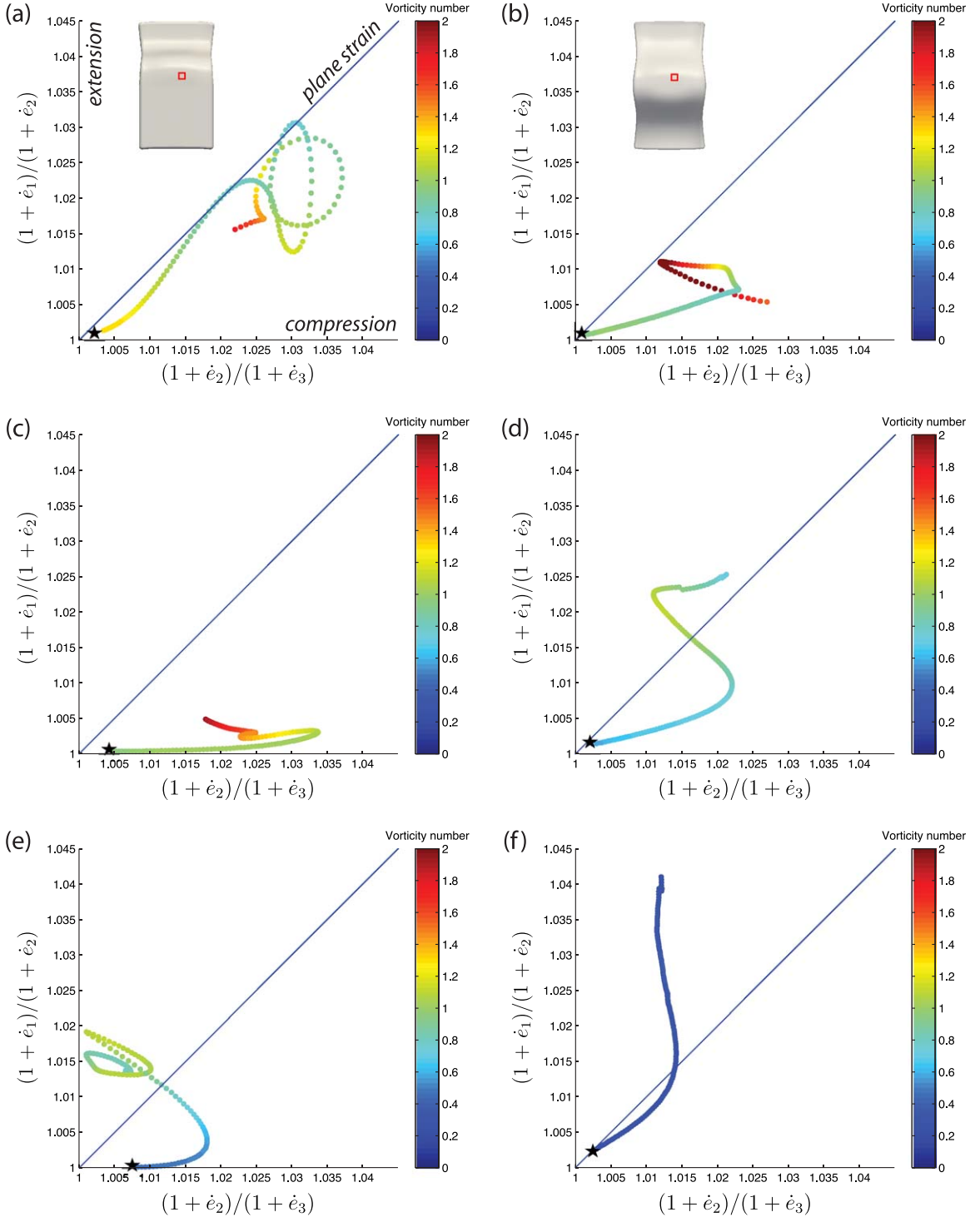

Figure 13. "Flinn-type" diagram (inspired by *Flinn* [1962]) to visualize the type of deformation a polycrystal undergoes in the subslab mantle during subduction ((left) single sided; (right) double sided; (a and b) topmost polycrystal; (c and d) middle; (e and f) bottommost polycrystal in the column). The $x = y$ line corresponds to plane strain, the horizontal axis ($y = 0$) to uniaxial compression, and the vertical axis ($x = 0$) to uniaxial extension. The points represent the time steps (starting point marked by black star) and are color coded by the vorticity number, . In plane strain ($x = y$), $= 0$ for pure shear, $= 1$ is consistent with simple shear, and > 1 signifies deformation in which vorticity dominates over shear. Note the difference in deformation patterns between single-sided and double-sided subduction.

5. Conclusions

[50] We present an integrated model to simulate history-dependent upper mantle LPO development and resulting shear wave splitting. We compare results to observations from the double-sided Molucca Sea subduction system. Incorporating the entire strain history of the deformed mantle is essential, as LPO textures are a function of the magnitude of accumulated finite strain, but also the variation of flow velocity gradients along the path a volume of rock has traveled. The Molucca Sea subduction system offers an ideal case study for two reasons: (1) It is fairly young and the slab has not been stagnating at the bottom of the mantle transition zone for long. Thus, early textures from the slab's descent, which we are able to simulate in our models, have not yet been overprinted by subsequent steady state flow. (2) It allows us to test the significance of the double-sided geometry, or, in more generic terms, the significance of a rear barrier to achieve trench-parallel subslab mantle flow.

[51] Our results show that trench-parallel fast directions can be produced without such a barrier and that this is in large part due to extension through axial compression and pure shear deformation in the subslab mantle, and not exclusively due to trench-parallel mantle flow. However, in the double-sided subduction model, trench-parallel anisotropy is significantly stronger and in no small part due to the mantle flowing outward and escaping the sinking microplate, as surmised by *Di Leo et al*. [2012a] in their shear wave splitting study of the Sangihe subduction zone.

[52] The results presented here are in good agreement with most models and shear wave splitting observations of trench-perpendicular mantle wedge flow, with a horizontal flow toward the trench, supraslab shear layers of strong LPO, and an effectively isotropic mantle wedge interior. At the edge of the slab, toroidal return flow from the subslab region toward the mantle wedge accommodates subduction from an early stage onward.

[53] Our study shows that measurements of shear wave splitting under the assumption of deformation dominated by the motion of dislocations belonging to the (010)[100] slip system may be used to study flow in the upper mantle, even in such complex settings as subduction zones, but several deformation mechanisms contribute in varying amounts, and caution is required. Additional modeling of strain-history-dependent texture development can improve our understanding of the upper mantle as it responds to subduction.

Acknowledgments

[54] The research leading to these results has received funding from Crystal2Plate, an FP7-funded Marie Curie Action under grant agreement PITN-GA-2008-215353, and from the European Research Council under the European Union's Seventh Framework Program (FP7/2007–2013)/ERC grant agreement 240473 "CoMITAC." Z.H.L. received funding from the National Natural Science Foundation of China (41304071).

References

Avé-Lallemant, H. G. (1975), Mechanisms of preferred orientations in olivine in tectonite peridotites, *Geology*, *3*, 653–656.

Babuška, V., and M. Cara (1991), *Seismic Anisotropy in the Earth*, Kluwer Acad., Norwell, Mass.

Bellahsen, N., C. Faccenna, and F. Funiciello (2005), Dynamics of subduction and plate motion in laboratory experiments: Insights into the ''plate tectonics'' of the Earth, *J. Geophys. Res.*, *110*, B01401, doi:10.1029/2004JB002999.

Blackman, D. K., and J.-M. Kendall (2002), Seismic anisotropy in the upper mantle: 2. Predictions for current plate boundary flow models, *Geochem. Geophys. Geosyst.*, *3*(9), 8602, doi:10.1029/2001GC000247.

Blackman, D. K., H.-R. Wenk, and J.-M. Kendall (2002), Seismic anisotropy of the upper mantle: 1. Factors that affect mineral texture and effective elastic properties, *Geochem. Geophys. Geosyst.*, *3*(9), 8601, doi:10.1029/2001GC000248.

Bonnin, M., A. Tommasi, R. Hassani, S. Chevrot, J. Wookey, and G. Barruol (2012), Numerical modelling of the upper-mantle anisotropy beneath a migrating strike-slip plate boundary: The San Andreas Fault system, *Geophys. J. Int.*, *191*, 436–458, doi:10.1111/j.1365-246X.2012.05650.x.

Boudier, F., and A. Nicolas (1995), Nature of the Moho transition zone in the Oman ophiolite, *J. Petrol.*, *36*, 777–796.

Buttles, J., and P. Olson (1998), A laboratory model of subduction zone anisotropy, *Earth Planet. Sci. Lett.*, *164*, 245–262.

Bystricky, M., K. Kunze, L. Burlini, and J. P. Burg (2000), High shear strain of olivine aggregates: Rheological and seismic consequences, *Science*, *290*(5496), 1564–1567.

Capitanio, F. A., and M. Faccenda (2012), Complex mantle flow around heterogeneous subducting oceanic plates, *Earth Planet. Sci. Lett.*, *353–354*, 29–37.

Capitanio, F. A., and G. Morra (2012), The bending mechanics in a dynamic subduction system: Constraints from numerical modelling and global compilation analysis, *Tectonophysics*, *522–523*, 224–234.

Carrez, P., A. M. Walker, A. Metsue, and D. Cordier (2008), Evidence from numerical modelling for 3D spreading of [001] screw dislocations in Mg_2SiO_4 forsterite, *Philos. Mag.*, *88*, 2477–2485.

Carter, N. L. (1976), Steady state flow of rock, *Rev. Geophys.*, *14*, 301–360.

Civello, S., and L. Margheriti (2004), Toroidal mantle flow around the Calabrian slab (Italy) from SKS splitting, *Geophys. Res. Lett.*, *31*, L10601, doi:10.1029/2004GL019607.

Couvy, H., D. J. Frost, F. Heidelbach, K. Nyilas, T. Ungár, S. Mackwell, and P. Cordier (2004), Shear deformation

experiments of forsterite at 11 GPa—1400° in the multianvil apparatus, *Eur. J. Mineral.*, *16*(6), 877–889.
Currie, C. A., J. F. Cassidy, R. D. Hyndman, and M. G. Bostock (2004), Shear wave anisotropy beneath the Cascadia subduction zone and western North American craton, *Geophys. J. Int.*, *157*(1), 341–353.
Dawson, P. R., and H.-R. Wenk (2000), Texturing of the upper mantle during convection, *Philos. Mag. A*, *80*(3), 573–598.
Di Giuseppe, E., J. van Hunen, F. Funiciello, C. Faccenna, and D. Giardini (2008), Slab stiffness control of trench motion: Insights from numerical models, *Geochem. Geophys. Geosyst.*, *9*, Q02014, doi:10.1029/2007GC001776.
Di Leo, J. F., J. Wookey, J. O. S. Hammond, J.-M. Kendall, S. Kaneshima, H. Inoue, T. Yamashina, and P. Harjadi (2012a), Deformation and mantle flow beneath the Sangihe subduction zone from seismic anisotropy, *Phys. Earth Planet. Int.*, *194–195*, 38–54, doi:10.1016/j.pepi.2012.01.008.
Di Leo, J. F., J. Wookey, J. O. S. Hammond, J.-M. Kendall, S. Kaneshima, H. Inoue, T. Yamashina, and P. Harjadi (2012b), Mantle flow in regions of complex tectonics: Insights from Indonesia, *Geochem. Geophys. Geosyst.*, *13*, Q12008, doi:10.1029/2012GC004417.
Dick, H. J. B., R. L. Fisher, and W. B. Bryan (1984), Mineralogic variability of the uppermost mantle along mid-ocean ridges, *Earth Planet. Sci. Lett.*, *69*, 88–106.
Djajadihardja, Y. S., A. Taira, H. Tokuyama, K. Aoike, C. Reichert, M. Block, H. U. Schluter, and S. Neben (2004), Evolution of an accretionary complex along the north arm of the island of Sulawesi, Indonesia, *Isl. Arc*, *13*, 1–17.
Druken, K. A., M. D. Long, and C. Kincaid (2011), Patterns in seismic anisotropy driven by rollback subduction beneath the High Lava Plains, *Geophys. Res. Lett.*, *38*, L13310, doi:10.1029/2011GL047541.
Faccenda, M., and F. A. Capitanio (2012), Development of mantle seismic anisotropy during subduction-induced 3-D flow, *Geophys. Res. Lett.*, *39*, L11305, doi:10.1029/2012GL051988.
Faccenda, M., and F. A. Capitanio (2013), Seismic anisotropy around subduction zones: Insights from three-dimensional modeling of upper mantle deformation and SKS splitting calculations, *Geochem. Geophys. Geosyst.*, *14*, 243–262, doi:10.1029/2012GC004451.
Falus, G., A. Tommasi, and V. Soustelle (2011), The effect of dynamic recrystallization on olivine crystal preferred orientations in mantle xenoliths deformed under varied stress conditions, *J. Struct. Geol.*, *33*, 1528–1540.
Flinn, D. (1962), On folding during three-dimensional progressive deformation, *Q. J. Geol. Soc. London*, *118*, 385–428.
Funiciello, F., M. Moroni, C. Piromallo, C. Faccenna, A. Cenedese, and H. A. Bui (2006), Mapping mantle flow during retreating subduction: Laboratory models analyzed by feature tracking, *J. Geophys. Res.*, *111*, B03402, doi:10.1029/2005JB003792.
Funiciello, F., A. Heuret, S. Lallemand, E. Di Giuseppe, and T. W. Becker (2008), Trench migration, net rotation and slab-mantle coupling, *Earth Planet. Sci. Lett.*, *271*, 233–240.
Gudmundsson, Ó., and M. Sambridge (1998), A regionalized upper mantle (RUM) seismic model, *J. Geophys. Res.*, *103*, 7121–7136.
Gutscher, M.-A., W. Spakman, H. Bijwaard, and E. R. Engdahl (2000), Geodynamics of flat subduction: Seismicity and tomographic constraints from the Andean margin, *Tectonics*, *19*, 814–833.
Hall, C. E., K. M. Fischer, E. M. Parmentier, and D. K. Blackman (2000), The influence of plate motions on three-dimensional back arc mantle flow and shear wave, *J. Geophys. Res.*, *105*, 28,009–28,033.
Hall, R. (1997), Cenozoic plate tectonic reconstructions of SE Asia, *Geol. Soc. Spec. Publ.*, *126*, 11–23.
Hall, R., and G. J. Nichols (1990), Terrane amalgamation in the Philippine Sea margin, *Tectonophysics*, *181*, 207–222.
Hammond, J. O. S., J. Wookey, S. Kaneshima, H. Inoue, T. Yamashina, and P. Harjadi (2010), Systematic variation in anisotropy beneath the mantle wedge in the Java-Sumatra subduction system from shear-wave splitting, *Phys. Earth Planet. Int.*, *178*, 189–201.
Jadamec, M. A., and M. I. Billen (2010), Reconciling surface plate motions with rapid three-dimensional mantle flow around a slab edge, *Nature*, *465*, 338–342, doi:10.1038/nature09053.
Jadamec, M. A., and M. I. Billen (2012), The role of rheology and slab shape on rapid mantle flow: Three-dimensional numerical models of the Alaska slab edge, *J. Geophys. Res.*, *117*, B02304, doi:10.1029/2011JB008563.
Jaffe, L. A., D. R. Hilton, T. P. Fischer, and U. Hartono (2004), Tracing magma sources in an arc-arc collision zone: Helium and carbon isotope and relative abundance systematics of the Sangihe Arc, Indonesia, *Geochem. Geophys. Geosyst.*, *5*, Q04J10, doi:10.1029/2003GC000660.
Jaraslow, G. E., G. Hirth, and H. J. B. Dick (1996), Abyssal peridotite mylonites: Implications for grain-size sensitive flow and strain localization in the oceanic lithosphere, *Tectonophysics*, *256*, 17–37.
Jung, H., W. Mo, and H. W. Green (2009), Upper mantle seismic anisotropy resulting from pressure-induced slip transition in olivine, *Nat. Geosci.*, *2*, 73–77.
Kaminski, É., and N. M. Ribe (2001), A kinematic model for recrystallization and texture development in olivine polycrystals, *Earth Planet. Sci. Lett.*, *189*, 253–267.
Kaminski, É., and N. M. Ribe (2002), Timescales for the evolution of seismic anisotropy in mantle flow, *Geochem. Geophys. Geosyst.*, *3*(8), 1051, doi:10.1029/2001GC000222.
Karato, S. (1988), The role of recrystallization in the preferred orientation of olivine, *Phys. Earth Planet. Int.*, *51*, 107–122.
Kendall, J.-M., and C. J. Thomson (1993), Seismic modelling of subduction zones with inhomogeneity and anisotropy—I. Teleseismic P-wavefront tracking, *Geophys. J. Int.*, *112*, 39–66.
Kincaid, C., and R. W. Griffiths (2003), Laboratory models of the thermal evolution of the mantle during rollback subduction, *Nature*, *425*, 58–62.
Kincaid, C., and P. Olson (1987), An experimental study of subduction and slab migration, *J. Geophys. Res.*, *92*, 13,832–13,840.
Kneller, E. A., and P. E. van Keken (2007), Trench-parallel flow and seismic anisotropy in the Mariana and Andean subduction systems, *Nature*, *450*(7173), 1222–1225, doi:10.1038/nature06429.
Lassak, T. M., M. J. Fouch, C. E. Hall, and E. Kaminski (2006), Seismic characterization of mantle flow in subduction systems: Can we resolve a hydrated mantle wedge?, *Earth Planet. Sci. Lett.*, *243*, 632–649.
Lay, T. (1994), The fate of descending slabs, *Annu. Rev. Earth Planet.*, *22*, 33–61.
Lebensohn, R. A., and C. N. Tomé (1993), A self-consistent anisotropic approach for the simulation of plastic deformation and texture development of polycrystals: Application to

zirconium alloys, *Acta Metall. Mater.*, *41*(9), 2611–2624, doi:10.1016/0956–7151(93)90130-K.
Li, Z.-H., and N. M. Ribe (2012), Dynamics of free subduction from 3-D boundary element modeling, *J. Geophys. Res.*, *117*, B06408, doi:10.1029/2012JB009165.
Long, M. D. (2013), Constraints on subduction geodynamics from seismic anisotropy, *Rev. Geophys.*, *51*, 76–112.
Long, M. D., and P. G. Silver (2008), The subduction zone flow field from seismic anisotropy: A global view, *Science*, *319*, 315–318.
Long, M. D., and P. G. Silver (2009), Mantle flow in subduction systems: The subslab flow field and implications for mantle dynamics, *J. Geophys. Res.*, *114*, B10312, doi:10.1029/2008JB006200.
Lowman, J. P., L. T. Piñero-Feliciangeli, J.-M. Kendall, and M. Hosein Shahnas (2007), Influence of convergent plate boundaries on upper mantle flow and implications for seismic anisotropy, *Geochem. Geophys. Geosyst.*, *8*, Q08007, doi:10.1029/2007GC001627.
Lynner, C., and M. D. Long (2013), Sub-slab seismic anisotropy and mantle flow beneath the Caribbean and Scotia subduction zones: Effects of slab morphology and kinematics, *Earth Planet. Sci. Lett.*, *361*, 367–378.
Macpherson, C. G., E. J. Forrde, R. Hall, and M. F. Thirlwall (2003), Geochemical evolution of magmatism in an arc-arc collision: The Halmahera and Sangihe arcs, eastern Indonesia, *Geol. Soc. Spec. Publ.*, *219*, 207–220.
Mainprice, D. (2007), Seismic anisotropy of the deep Earth from a mineral and rock physics perspective, *Treatise Geophys.*, *2*, 437–492.
Mainprice, D., and P. G. Silver (1993), Interpretation of SKS waves using samples from the continental lithosphere, *Phys. Earth Planet. Int.*, *78*, 257–280.
Mainprice, D., M. Humbert, and F. Wagner (1990), Phase-transformations and inherited lattice preferred orientations—Implication for seismic properties, *Tectonophysics*, *180*(2–4), 213–228.
McKenzie, D. (1979), Finite deformation during fluid flow, *Geophys. J. R. Astron. Soc.*, *58*, 689–715.
McKenzie, D. P. (1969), Speculations on the consequences and causes of plate motions, *Geophys. J. R. Astron. Soc.*, *18*, 1–32.
Morley, A. M., G. W. Stuart, J.-M. Kendall, and M. Reyners (2006), Mantle wedge anisotropy in the Hikurangi subduction zone, central North Island, New Zealand, *Geophys. Res. Lett.*, *33*, L05301, doi:10.1029/2005GL024569.
Müller, C., B. Bayer, A. Eckstaller, and H. Miller (2008), Mantle flow in the South Sandwich subduction environment from source-side shear wave splitting, *Geophys. Res. Lett.*, *35*, L03301, doi:10.1029/2007GL032411.
Nicolas, A., F. Boudier, and A. M. Boullier (1973), Mechanisms of flow in naturally and experimentally deformed peridotites, *Am. J. Sci.*, *273*, 853–876.
Piñero-Feliciangeli, L. T., and J.-M. Kendall (2008), Sub-slab mantle flow parallel to the Caribbean plate boundaries: Inferences from SKS splitting, *Tectonophysics*, *462*, 22–34.
Piromallo, C., T. W. Becker, F. Funiciello, and C. Faccenna (2006), Three-dimensional instantaneous mantle flow induced by subduction, *Geophys. Res. Lett.*, *33*, L08304, doi:10.1029/2005GL025390.
Polet, J., P. G. Silver, S. Beck, T. Wallace, G. Zandt, S. Ruppert, R. Kind, and A. Rudloff (2000), Shear wave anisotropy beneath the Andes from the BANJO, SEDA, and PISCO experiments, *J. Geophys. Res.*, *105*, 6287–6304, doi:10.1046/j.1365-246X.2002.01630.x.
Raterron, P., E. Amiguet, J. Chen, L. Li, and P. Cordier (2009), Experimental deformation of olivine single crystals at mantle pressures and temperatures, *Phys. Earth Planet. Int.*, *172*, 74–83.
Raterron, P., J. Chen, L. Li, D. Weidner, and P. Cordier (2007), Pressure-induced slip-system transition in forsterite: Single-crystal rheological properties at mantle pressure and temperature, *Am. Mineral.*, *92*, 1436–1445.
Ribe, N. M. (1989), Seismic anisotropy and mantle flow, *J. Geophys. Res.*, *94*, 4213–4223.
Ribe, N. M. (2010), Bending mechanics and mode selection in free subduction: A thin-sheet analysis, *Geophys. J. Int.*, *180*, 559–576.
Russo, R. M., and P. G. Silver (1994), Trench-parallel flow beneath the Nazca plate from seismic anisotropy, *Science*, *263*, 1105–1111.
Schellart, W. P. (2004), Kinematics of subduction and subduction-induced flow in the upper mantle, *J. Geophys. Res.*, *109*, B07401, doi:10.1029/2004JB002970.
Schellart, W. P. (2008), Kinematics and flow patterns in deep mantle and upper mantle subduction models: Influence of the mantle depth and slab to mantle viscosity ratio, *Geochem. Geophys. Geosyst.*, *9*, Q03014, doi:10.1029/2007GC001656.
Silver, P. G., and W. W. Chan (1991), Shear wave splitting and subcontinental mantle deformation, *J. Geophys. Res.*, *96*, 16,429–16,454.
Silver, P. G., and M. K. Savage (1994), The interpretation of shear wave splitting parameters in the presence of two anisotropic layers, *Geophys. J. Int.*, *119*, 949–963.
Stegman, D. R., J. Freeman, W. P. Schellart, L. Moresi, and D. May (2006), Influence of trench width on subduction hinge retreat rates in 3-D models of slab rollback, *Geochem. Geophys. Geosyst.*, *7*(3), Q03012, doi:10.1029/2005GC001056.
Stegman, D. R., R. Farrington, F. A. Capitanio, and W. P. Schellart (2010), A regime diagram for subduction styles from 3-D numerical models of free subduction, *Tectonophysics*, *483*, 29–45.
Tackley, P. J. (2008), Layer cake or plum pudding?, *Nat. Geosci.*, *1*, 157–158, doi:10.1038/ngeo134.
Tatsumi, Y., M. Murasaki, E. M. Arsadi, and S. Nohda (1991), Geochemistry of quaternary lavas from NE Sulawesi: Transfer of subduction components into the mantle wedge, *Contrib. Mineral. Petrol.*, *107*, 137–149.
Taylor, G. I. (1938), Plastic strain in metals, *J. Inst. Met.*, *32*, 307–324.
Tommasi, A. (1998) Forward modeling of the development of seismic anisotropy in the upper mantle, *Earth Planet. Sci. Lett.*, *160*(1–2), 1–13.
Tommasi, A., D. Mainprice, G. Canova, and Y. Chastel (2000), Viscoplastic self-consistent and equilibrium-based modeling of olivine lattice preferred orientations: Implications for the upper mantle seismic anisotropy, *J. Geophys. Res.*, *105*, 7893–7908.
van der Hilst, R. D., E. R. Engdahl, W. Spakman, and G. Nolet (1991), Tomographic imaging of subducted lithosphere below northwest Pacific island arcs, *Nature*, *353*, 37–43.
von Mises, R. (1928), Mechanik der plastischen Formänderung von Kristallen, *Z. Angew. Math. Mech.*, *8*, 161–185.
Walker, A. M., and J. Wookey (2012), MSAT: A new toolkit for the analysis of elastic and seismic anisotropy, *Comput. Geosci.*, *49*, 81–90.
Walker, A. M., P. Carrez, and P. Cordier (2010), Atomic-scale models of dislocation cores in minerals: Progress and prospects, *Mineral. Mag.*, *74*(3), 381–413.

Walker, A. M., A. M. Forte, J. Wookey, A. Nowacki, and J.-M. Kendall (2011), Elastic anisotropy of D'' predicted from global models of mantle flow, *Geochem. Geophys. Geosyst.*, *12*, Q10006, doi:10.1029/2011GC003732.

Wenk, H.-R., and C. N. Tomé (1999), Modeling dynamic recrystallization of olivine aggregates deformed in simple shear, *J. Geophys. Res.*, *104*, 25,513–25,527.

Wenk, H.-R., K. Bennett, G. R. Canova, and A. Molinari (1991), Modelling plastic deformation of peridotite with the self-consistent theory, *J. Geophys. Res.*, *96*, 8337–8349.

Zhang, S., and S. Karato (1995), Lattice preferred orientation of olivine aggregates deformed in simple shear, *Nature*, *375*, 774–777.

Zhong, S., M. Gurnis, and L. Moresi (1998), Role of faults, nonlinear rheology, and viscosity structure in generating plates from instantaneous mantle flow models, *J. Geophys. Res.*, *103*, 15,255–15,268.

Zhang, S., S. Karato, J. Fitz Gerald, U. H. Faul, and Y. Zhou (2000), Simple shear deformation of olivine aggregates, *Tectonophysics*, *316*, 133–152.